Journal Article

Design and analysis of curved wire for biomedical device applications

Rafiei Anamagh, M., Ullah, M. and Gavin, G.

Taylor & Francis
Taylor & Francis Group

International Journal for Computational Methods in Engineering Science and Mechanics

ISSN: 1550-2287 (Print) 1550-2295 (Online) Journal homepage: www.tandfonline.com/journals/ucme20

Design and analysis of curved wire for biomedical device applications

Mirmeysam Rafiei Anamagh, Mudaser Ullah & Graham Gavin

To cite this article: Mirmeysam Rafiei Anamagh, Mudaser Ullah & Graham Gavin (2025) Design and analysis of curved wire for biomedical device applications, International Journal for Computational Methods in Engineering Science and Mechanics, 26:6, 363-374, DOI: 10.1080/15502287.2025.2541117

To link to this article: https://doi.org/10.1080/15502287.2025.2541117

INTERNATIONAL JOURNAL FOR COMPUTATIONAL METHODS IN ENGINEERING SCIENCE AND MECHANICS
2025, VOL. 26, NO. 6, 363–374
https://doi.org/10.1080/15502287.2025.2541117

Design and analysis of curved wire for biomedical device applications

Mirmeysam Rafiei Anamagh[a], Mudaser Ullah[b], and Graham Gavin[b]

[a]Faculty of Arts, Computing and Engineering, Wrexham University, Wrexham, UK; [b]School of Mechanical Engineering, Technological University Dublin, Ireland

ABSTRACT

In this study, the dynamic behavior of curved wires is investigated and optimized with a focus on biomedical applications. To solve the integral boundary value problem of the curved wire, a spectral Chebyshev approach is developed in conjunction with the first-order shear deformation theory for beams. The wire shapes are categorized into two main groups: (i) with curvature and (ii) without curvature. In the former category, the curved segment is located in the middle of the wire, flanked by two straight segments, resulting in a complex geometric equation. The proposed method is validated by comparing the obtained natural frequencies with those reported in the literature and results from the finite element method. The results for different boundary conditions and various geometric properties show excellent agreement with both the literature and finite element method. Furthermore, a design process is conducted to optimize the maximum displacement response of the wire distal tip relative to the base excitation amplitude. This process involves varying the length ratios of the tapered wire, defined as design variables, for different lengths of straight wires and various curvature amounts of curved wires. The design results indicate that the ratio of distal tip displacement to base excitation amplitude can be increased by up to 600% for straight wires and 240% for curved wires at an excitation frequency of 40 kHz.

KEYWORDS

Vibration; smart materials; biomedical; numerical method; ultrasonic; wire

1. Introduction

Cardiovascular diseases encompass a range of conditions affecting the arteries and the broader cardiovascular system, with atherosclerosis being a common and severe manifestation. This condition involves the buildup of plaques within arterial walls, which restrict oxygen-rich blood flow to downstream tissues. As the disease progresses, these plaques often become calcified and composed of rigid fibrous tissue and calcium deposits, posing significant challenges for treatment [1]. Minimally invasive endovascular procedures, such as balloon angioplasty and stent implantation, are widely employed to address such blockages. These procedures rely on guidewires and catheters as primary tools, with the guidewire threaded through the catheter to navigate blood vessels and reach the target site. While effective, the slender and flexible design of guidewires, optimized to minimize trauma, often limits their ability to penetrate heavily calcified plaques.

To address the limitations of conventional guidewires in treating advanced atherosclerotic lesions, a promising solution involves applying high-frequency mechanical vibrations (amplitude: 0–50 μm; frequency: 20–100 kHz) to the guidewire's proximal end using a piezoelectric transducer [2]–[5]. These vibrations propagate along the wire, enabling the distal tip to perform controlled reciprocating motions that disrupt and ablate calcified material. By enhancing the guidewire's capability to penetrate rigid plaques, this innovative approach has the potential to improve the efficacy of endovascular procedures, addressing a critical need in cardiovascular treatment while ensuring device reliability and patient safety.

It is evident that modeling and simulating wires at these high frequencies can be beneficial in understanding their behavior and improving their efficiency in such applications. In recent years, there has been increasing attention on studying guidewires under real environmental conditions within blood vessels. To reduce the trial-and-error

CONTACT Mirmeysam Rafiei Anamagh meysam.anamagh@wrexham.ac.uk Faculty of Arts, Computing and Engineering, Wrexham University, Wrexham, UK.

Supplemental data for this article can be accessed online at https://doi.org/10.1080/15502287.2025.2541117.

costs in research, numerical methods have been developed for simulating and optimizing biomedical devices. Tang et al. conducted research to simulate the interaction between guidewires, with both straight and curved geometries, and the vessel [6]. Alderliesten et al. created an algorithm capable of simulating both completely straight and intrinsically curved guidewires by accounting for applied translations and rotations [7]. Zhang et al. [8] investigated the dynamic behavior of the wire within the ultrasonic frequency range of 20–25 kHz, under a specific 30° angle. Berti et al. studied the functionality of NiTi material wires with closed sections using the finite element method [9]. In a separate study by Konh et al., a three-dimensional (3D) finite element (FE) model of a steerable cannula was created to illustrate the potential of using SMA wires as actuators for bending the surgical instrument [10]. Chapman et al. investigate the torsional behavior of NiTi wires using both one-dimensional and three-dimensional modeling approaches [11]. However, a significant drawback of the finite element method is its high computational cost, which can lead to extended design process times. Furthermore, to date, most numerical studies have focused on the static behavior of wires. For example, Gannoun et al. examined the forces generated by a superelastic NiTi orthodontic archwire during the tooth alignment phase [12].

In this study, we investigate the dynamic behavior of a curved wire within an anatomical environment. To achieve this, we developed a novel numerical approach called spectral Chebyshev method (SC) to solve the wire's equation of motion. The integral boundary value problem is formulated using Hamilton's principle, in conjunction with the first order shear deformation theory (FSDT) for beams. To validate the proposed method, various studies are conducted by comparing results with those from existing literature and commercial software. The findings demonstrate that the spectral Chebyshev method accurately determines the natural frequencies of the defined wire geometries. Additionally, several parametric studies are conducted to explore the effects of geometric parameters on the wire's steady-state response. Finally, an optimization study is performed to determine the optimum geometric parameters for both straight and curved wires, considering the presence of taper sections in the wire geometry.

2. Theoretical model

2.1. Problem geometry and governing equations

The wire geometry depicted in Figure 1a is composed of two primary sections, each of which can be further expanded for investigation. In part (I), a straight wire of length L_I is depicted. The endpoint of part (I) serves as the starting point for part (II). Part (II) represents a curved wire, which can exhibit either constant curvature (a circular shape) or variable curvature ($y = y(x)$). In the case of constant curvature, the radius of the wire remains consistent, denoted as $R(s) = R$. Alternatively, when the curvature of the curved wire follows the equation y, it can be expressed as

$$\frac{1}{R} = \frac{|y''|}{|\sqrt[3/2]{1+y'^2}|} \tag{1}$$

In this study, y' and y'' represent the first and second derivatives of function y with respect to x, respectively. Three equations for y are defined, as illustrated in Figure 1b–d. It's worth noting that f is equal to h/L_{II}, where h denotes the arch rise and L_{II} indicates the span length. Additionally, the slenderness ratio (SR) can be expressed as $L_{II}/\sqrt{I/A}$, where I and A represent the area moment of inertia and cross-sectional area of the wire, respectively. Also, parameters c_1 and c_2 can be calculated as:

$$c_1 = f/[1 - \sin(\epsilon c_2)] \tag{2}$$

$$c_2 = \pi/(1 + 2\epsilon) \tag{3}$$

The wire's deformation can be determined by employing the first-order shear deformation theory for

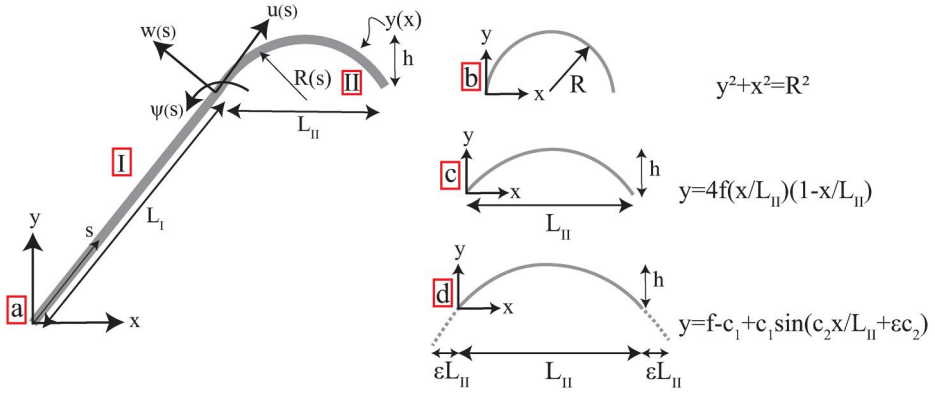

Figure 1. Schematic of the wire.

beams. As illustrated in Figure 1a, three degrees of freedom are defined: $u(s)$, $w(s)$, and $\psi(s)$, representing tangential, radial, and rotational displacements, respectively. The total displacements can be expressed as:

$$U(s,t) = u(s,t) + \frac{w(s,t)}{R} \tag{4}$$

$$W(s,t) = w(s,t) \tag{5}$$

$$\boldsymbol{\psi}(s,t) = \psi(s,t) - \frac{\mathrm{d}w(s,t)}{\mathrm{d}s} - \frac{\mathrm{d}u(s,t)}{\mathrm{d}s} \tag{6}$$

It should be noted that w/R and $\mathrm{d}w/\mathrm{d}s$, are the tangential displacement due to the radial displacement along the s coordinate and total rotation, respectively. Based on the deformation equations, the strain energy can be written as

$$\begin{aligned} V = &\frac{1}{2}\int_L EA(s)\left(\frac{\partial U(s,t)}{\partial s}\right)^2 \mathrm{d}s \\ &+ \frac{1}{2}\int_L k_q GA(s)\left(\frac{\partial \boldsymbol{\psi}(s,t)}{\partial s}\right)^2 \mathrm{d}s \\ &+ \frac{1}{2}\int_L EI(s)\left(\frac{\partial W(s,t)}{\partial s}\right)^2 \mathrm{d}s \end{aligned} \tag{7}$$

Here, E, G, and k_q represent the modulus of elasticity, shear modulus, and the shear correction factor set to 5/6, respectively. The kinetic energy of the wire can be written as

$$\begin{aligned} T = &\frac{1}{2}\int_L m(s)\left(\frac{\partial U(s,t)}{\partial t}\right)^2 \mathrm{d}s + \frac{1}{2}\int_L J_s\left(\frac{\partial \boldsymbol{\psi}(s,t)}{\partial t}\right)^2 \mathrm{d}s \\ &+ \frac{1}{2}\int_L m(s)\left(\frac{\partial W(s,t)}{\partial t}\right)^2 \mathrm{d}s \end{aligned} \tag{8}$$

The mass moment of inertia density, $J(s)$, is related to the area moment of inertia, $I(s)$, and the beam material density, $\rho(s)$, along the central line of the curvilinear beam by the equation $J(s) = \rho(s)I(s)$. Using Hamilton's principle the stiffness (K) and mass (M) matrices can be calculated based on the strain and kinetic energies depicted in Eqs. (7) and (8), respectively

$$K = \int_L \begin{bmatrix} \frac{\partial}{\partial s} & -\frac{1}{R} & 0 \\ \frac{1}{R} & \frac{\partial}{\partial s} & 0 \\ 0 & -1 & \frac{\partial}{\partial s} \end{bmatrix} \begin{bmatrix} EA(s) & 0 & 0 \\ 0 & k_q GA(s) & 0 \\ 0 & 0 & EI(s) \end{bmatrix} \begin{bmatrix} \frac{\partial}{\partial s} & \frac{1}{R} & 0 \\ -\frac{1}{R} & \frac{\partial}{\partial s} & -1 \\ 0 & 0 & \frac{\partial}{\partial s} \end{bmatrix} \mathrm{d}s \tag{9}$$

$$M = \int_L \begin{bmatrix} \rho A & 0 & 0 \\ 0 & \rho A & 0 \\ 0 & 0 & J \end{bmatrix} \mathrm{d}s \tag{10}$$

3. Spectral Chebyshev method

In this section, a meshless approach known as the spectral Chebyshev approach is explained for calculating the stiffness and mass matrices described in Eqs. (9) and (10). In this study, the one-dimensional expression of the Chebyshev polynomials is utilized to discretize the function of displacement on the Gauss-Lobatto points used for discretizing the domain of the problem (s) [13], [14]. The one-dimensional expansion using Chebyshev polynomials can be written as:

$$q_k(s) = \sum_{i=1}^{N_s} a_{k_{i-1}} T_{i-1}(\zeta) \tag{11}$$

where the coefficients a_k represent the expansion in the domain s, which is discretized by N_s Gauss–Lobatto sampling points. It should be noted that k represents each degree of freedom of displacement ($q_1 = U, q_2 = W, q_3 = \psi$). T denotes the Chebyshev polynomials as defined in Eq. (12). These polynomials are recursive, orthogonal, and exhibit exponential convergence, effectively mapping the spatial domain $[0, L_s]$ onto the interval $\zeta = [-1, 1]$.

$$T_i(\zeta) = \cos(k\cos^{-1}(\zeta)) \qquad k = 0, 1, \ldots, N_s - 1 \tag{12}$$

Consequently, mapped deflection can be rewritten as

$$\mathbf{q}_k = \Gamma_B a_k \tag{13}$$

Here, $\mathbf{q}_k$ represents displacements in spatial coordinates. Γ_B denotes the backward matrix, which connects these displacements to the coefficients of Chebyshev polynomials, and it can be generated from the Chebyshev polynomials at the sampling points. To derive the system matrices, one essential operation is to compute the derivative and integral matrices. These can be obtained by calculating the derivative and integral of Chebyshev polynomials at the sampling points. Hence, the coefficients of the derivative expansion can be related to a_k as follows:

$$b_k = D a_k \tag{14}$$

Thus, the derivative matrix at sampling points can be computed as

$$\frac{\partial \mathbf{q}_k}{\partial \zeta} = \Gamma_B b_k = \Gamma_b D a_k = \Gamma_B D \Gamma_B^{-1} \mathbf{q}_k = Q \mathbf{q}_k \tag{15}$$

Here, Q represents the differential matrix. Utilizing the inner product definition, the integral matrix (V) can be generated using the Chebyshev polynomials, similar to the derivative process, and can be employed as

$$\int_s fg\mathrm{d}s = \mathbf{f}^T\mathbf{V}\mathbf{g} \tag{16}$$

where $\mathbf{f}$ and $\mathbf{g}$ represent the values of the functions f and g at the sampling points, respectively. $\mathbf{V}$ denotes the inner product matrix. To enforce the essential boundary condition ($\beta_k\mathbf{q}_k = 0$), $\mathbf{P}_k$ can be obtained by performing singular value decomposition on β_k. Therefore, the system matrices can be rewritten by applying boundary conditions on Eqs. (9) and (10) as

$$\mathbf{K} = \mathbf{P}^T K\mathbf{P} \quad \mathbf{M} = \mathbf{P}^T M\mathbf{P} \tag{17}$$

Subsequently, natural frequencies (ω_n) and the corresponding mode shapes ($\mathbf{u}$) can be determined by solving the following eigenvalue problem:

$$(\mathbf{K} - \omega_n^2\mathbf{M})\mathbf{u}_n e^{i\omega t} = \mathbf{f}e^{i\omega t} \tag{18}$$

In addition to the Eq. (18), the frequency response of the wire can be calculated as

$$u = \mathbf{f}/(-\omega^2\mathbf{M} + (1 + jc)\mathbf{K}) \tag{19}$$

Here, $\mathbf{f}$ represents the amplitude of the harmonic excitation force applied at the base of the wire, as indicated by the red arrow in the axial direction (s) in Figure 2, and is calculated as $\mathbf{f} = P'f$, where f is the force vector including the force amplitude at the base node. The parameter c represents the damping factor, and ω denotes the excitation frequency.

4. Optimization formulation

As part of this study, maximizing the displacement at the distal tip of the wire (δ_e) compared to the displacement at the base (δ_b), is crucial for enhancing the wire's functionality. This enhancement aims to improve the wire's ability to penetrate dense calcified plaques encountered *in vivo*. One approach to achieving the mentioned goal is to design the wire with a tapered section, which amplifies the input excitation amplitude and has the added benefit of increasing wire flexibility in the tortuous vasculature., as shown in Figure 2. Two key geometric parameters of the proposed wire can be optimized. As depicted in Figure 2, these parameters include the ratios of l_f/l_e and l_t/l_e. The total length of the wire (L_t) and the taper section angle (α) will be constant.

Therefore, the optimization problem can be written as

$$\begin{aligned} &\text{max.} && \delta_e/\delta_b = f(l_f/l_e, l_t/l_e) \\ &\text{s.t.} && \alpha = L_t = const. \end{aligned} \tag{20}$$

The optimization problem described above is approached as a constrained minimization, tackled using the built-in *fmincon* function in MATLAB's Optimization Toolbox, employing the Sequential Quadratic Programming (SQP) algorithm.

5. Validation study

To validate the precision of the developed spectral Chebyshev method, various case studies are conducted to obtain the natural frequencies of the wire and compare them with those reported in the literature and commercial finite element software (*ABAQUS*). The non-dimensional natural frequencies can be determined as

$$\overline{\omega} = \omega l^2\sqrt{\frac{\rho A}{EI}} \tag{21}$$

Also, three types of boundary conditions are defined presented in Table 1.

In the first step, the second part of the wire depicted in Figure 1b is investigated. This indicates that the entire wire is of curved type without any straight partition. The material properties are detailed in Table 2.

Also, geometry properties are presented in Table 3 for clamped-clamped (*CC*) and pinned-pinned (*PP*) boundary conditions.

Table 4 shows the obtained first three natural frequencies for two types of boundary conditions using the SC approach and compares them to those

Table 1. Three types of boundary conditions.

Hinged (H)	Pinned (P)	Clamped (C)
$u = 0$, $w = 0$, $\mathrm{d}\psi/\mathrm{d}s = 0$	$u = 0$, $w = 0$	$u = 0$, $w = 0$, $\psi = 0$

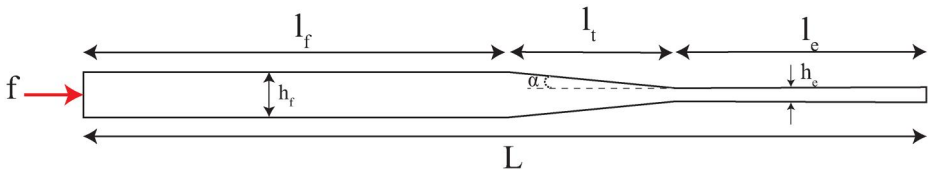

Figure 2. A design of a wire with a tapered section.

obtained in the literature. The results show an excellent match, demonstrating the accuracy of the presented spectral Chebyshev method.

In another validation study, we analyze the first three natural frequencies of a curved wire with parabolic and sinusoidal geometries, as shown in Figure 1c and d. For the parabolic wire, the boundary condition is set to hinged-hinged (HH), and for the sinusoidal wire, the boundary conditions are set to hinged-clamped (HC). Two variables are defined for these geometries as $f = h/L$ and $SR = L/\sqrt{I/A}$ which represent the arch rise to the span length and slenderness ratio, respectively. The mentioned parameter values are $(f = 0.3, SR = 75)$ and $(f = 0.1, SR = 100)$ for parabolic and sinusoidal geometries, respectively. The material properties are the same as in the previous case study (Table 2). The results, presented in Table 5, are compared to those in the literature. The results demonstrate the capability of the SC method to accurately obtain the natural frequencies of wires with complex geometry.

Table 2. Material properties of wire.

E	G	ρ	k_q
70 *Gpa*	$0.3k_q$/E	2777 kg/m^3	0.85

Table 3. Geometry properties of a curved wire for clamped-clamped and pinned-pinned boundary conditions.

BC	R/r	l/r	ϕ	RM	A m^2	I m^4
PP	15	23.56	90^o	0.75	4	0.01
CC	15.915	25	90^o	0.6366	1	0.0016

Table 4. The first three natural frequencies for a wire with two different boundary conditions and constant curvature.

	CC		PP	
Mode	SC	Ref. [15]	SC	Ref. [15]
1	36.70	36.70	29.28	29.28
2	42.26	42.26	33.30	33.31
3	82.23	82.23	67.12	67.12

Table 5. The first three natural frequencies for a wire with elliptical and sinusoidal.

	Parabolic(HH)		Sinusoidal(HC)	
Mode	SC	Ref. [15]	SC	Ref. [15]
1	21.17	21.76	56.07	56.08
2	54.95	55.49	66.15	66.05
3	100.25	100.70	113.47	113.41

The ultimate goal of this study is to develop an accurate approach for analyzing the wire shown in Figure 1a. To achieve this, the straight section of the structure will be incorporated into the curved part. The problem is divided into two parts, which are then coupled using the appropriate equations. This allows for the calculation of new mass and stiffness matrices as follows:

$$\mathbf{M} = \mathbf{P}^T \begin{bmatrix} M_1 & 0 \\ 0 & M_2 \end{bmatrix} \mathbf{P}, \quad \mathbf{K} = \mathbf{P}^T \begin{bmatrix} K_1 & 0 \\ 0 & K_2 \end{bmatrix} \mathbf{P} \tag{22}$$

Here, M_i and K_i are the mass and stiffness matrices derived for the i^{th} portion of the structure, respectively. P includes the coupling and boundary condition properties of the problem [16]. Table 6 presents the first ten natural frequencies (Hz) for three different case studies: (I) a straight wire without a curved portion, (II) a straight wire coupled to a quarter-circle curved portion (Figure 3a), and (IV) a straight wire coupled to a half-circle portion (Figure 3b). The geometric properties of the straight portion for all case studies are set to $L_1 = 1$ m and the cross-sectional radius is 0.215 mm. For the curved portion of the wire, the cross-section remains constant, with a radius of curvature set to 0.2 m. The elastic modulus and Poisson's ratio are 71.3 GPa and 0.3, respectively, with a density of 6450 kg/m^3 [17]. For this case study, two boundary conditions are considered: clamped-clamped (CC) and clamped-free (CF). The free boundary

Table 6. The first ten natural frequencies (Hz) are calculated for (I) the straight wire without a curved portion, (II) the straight wire coupled to The Quarter-circle portion, and (III) the straight wire coupled to the half-circle portion.

BC	(CC)						(CF)					
Case	(I)		(II)		(III)		(I)		(II)		(III)	
Mode	SC	FE	SC	FE	SC	FE	SC	FE	SC	FE	SC	FE
1	1.27	1.27	1.00	1.00	0.80	0.80	0.2	0.2	0.12	0.12	0.09	0.09
2	3.51	3.51	2.76	2.76	1.93	1.93	1.25	1.25	0.74	0.74	0.42	0.42
3	6.88	6.88	5.39	5.39	3.39	3.39	3.51	3.51	1.95	1.95	1.05	1.05
4	11.37	11.37	8.79	8.80	5.52	5.52	6.88	6.88	3.67	3.67	2.26	2.26
5	16.98	16.98	12.86	12.86	8.01	8.01	11.37	11.37	6.16	6.16	3.67	3.67
6	23.72	23.72	17.47	17.48	10.71	10.72	16.98	16.98	9.46	9.47	5.73	5.73
7	31.58	31.59	22.68	22.69	14.21	14.21	23.72	23.72	13.40	13.41	8.35	8.35
8	40.56	40.57	28.59	28.60	18.05	18.05	31.58	31.58	17.84	17.84	11.11	11.11
9	50.67	50.68	35.11	35.09	22.17	22.18	40.56	40.56	22.90	22.90	14.55	14.55
10	61.90	61.92	42.30	41.95	26.96	26.97	50.67	50.67	28.78	28.79	18.40	18.40

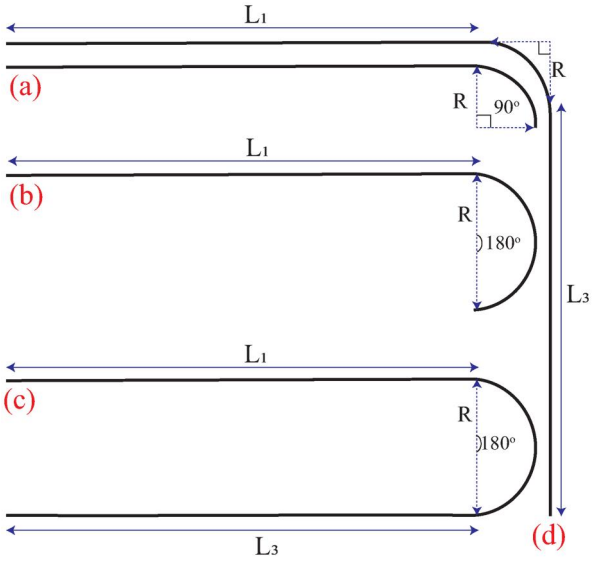

Figure 3. Geometry of wires: (a) straight with quarter-circle (b) straight with half-circle (c) half-circle with two straight (d) quarter-circle with two straight.

condition is applied to the endpoint of the curved portion of the wire (distal tip). The close agreement between the two methods suggests that the SC method can be confidently used for predicting the natural frequencies and other dynamic characteristics of complex structures, particularly in cases where traditional FEM might be more computationally intensive.

Considering the application of wires in medical devices, it is necessary to develop a numerical method capable of analyzing wires with the geometries shown in Figure 3c and d. The figure includes three main parts: two straight sections and one curved section. The system matrices can be calculated by expanding Eq. (22). The length of the straight parts is 1 m, and the wire diameter is set to 0.215 mm. Additionally, the radius of the curved portion is 0.2 m. Table 7 presents the first ten natural frequencies obtained for the geometries shown in Figure 3c and d. The results are compared to those obtained from commercial finite element software. Each geometry is analyzed under two boundary conditions: clamped-free (CF) and clamped-clamped (CC). The comparison indicates that the developed spectral Chebyshev approach can accurately capture the natural frequencies of the wire with complex geometries.

Subsequently, the spectral Chebyshev (SC) approach is developed to analyze a wire with a tapered cross-section, as illustrated in Figure 2. The geometric properties used in this case study are listed in Table 8. The frequency response of the wire is computed and compared against results obtained from the finite element method (FEM). For this case, the left edge of the wire is clamped. Figure 4 shows the frequency response of the wire for various lengths of the thicker section (L_f). The displacement is measured at the distal tip of the wire, while a 1 N harmonic excitation force is applied at the base across a frequency range of 30–40 kHz. The results from the proposed SC method are shown as solid lines, and the FEM results are represented by hollow circles. The structural damping coefficient is assumed to be $c = 0.021$. It is observed that the number of natural frequencies (identified by the peaks in the solid lines) within this frequency range decreases as the thicker section of the wire becomes longer. This case study demonstrates that the SC method can accurately predict the dynamic response of the wire at high frequencies. From a computational perspective, the SC method requires only 153 degrees of freedom, compared to 2800 for the FEM. This results in a 40-fold reduction in computation time on the same hardware, making the SC method highly advantageous for the optimization studies presented in the following sections.

Table 7. The first ten natural frequencies (Hz) of the wire with geometries shown in Figure 3c and d. Two boundary conditions are applied as clamped-clamped (CC) and clamped-free (CF).

BC	(CC)				(CF)			
Case	(c)		(d)		(c)		(d)	
Mode	SC	FE	SC	FE	SC	FE	SC	FE
1	0.2049	0.2048	0.6101	0.6095	0.0689	0.0689	0.0474	0.0474
2	0.7867	0.7861	0.9906	0.9897	0.0836	0.0835	0.1372	0.1371
3	1.1702	1.1691	1.9872	1.9853	0.3385	0.3384	0.6252	0.6247
4	2.1652	2.1635	2.7780	2.7753	0.7820	0.7814	1.0184	1.0172
5	2.9171	2.9146	4.1791	4.1754	1.2043	1.2031	2.0068	2.0049
6	4.1294	4.1266	5.4976	5.4926	2.1716	2.1697	2.8081	2.8049
7	5.4174	5.4132	7.2199	7.2140	2.9291	2.9262	4.1992	4.1951
8	6.7152	6.7109	9.1180	9.1105	4.1506	4.1472	5.5180	5.5119
9	8.5459	8.5401	11.1384	11.1300	5.4191	5.4140	7.2383	7.2313
10	10.1022	10.0960	13.5900	13.5800	6.7436	6.7383	9.1275	9.1179

Table 8. The geometry properties of the wire as shown in Figure 2.

L(mm)	l_t(mm)	h_f(mm)	h_c(mm)
1400	100	0.215	0.125

6. Parametric study and design

In this section, parametric and design studies are conducted to investigate the effect of geometry on the dynamic response of the wire. As stated in the introduction, the main objective of this work is to analyze the dynamic behavior of wires with potential biomedical applications. With recent advancements in biomedical devices and the growing use of ultrasonic

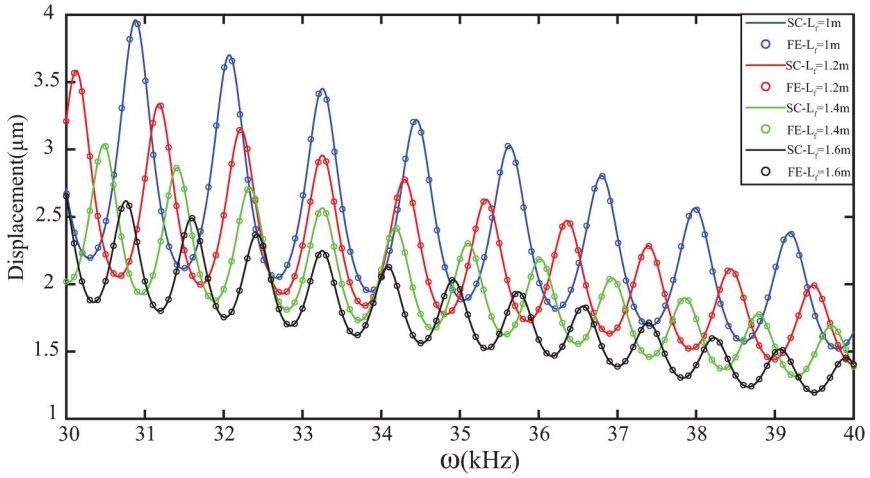

Figure 4. Comparison of the frequency response of a straight wire with different lengths using the presented SC and FE methods.

transducers, excitation frequencies in the ultrasonic range, typically between 20 kHz and 40 kHz, have become common, allowing for smaller excitation amplitudes. Accordingly, all case studies in this section are performed within the frequency range of 38–42 kHz.

This study aims to maximize the displacement at the distal tip of the wire within the specified frequency range. The key objective parameter is the steady-state, non-dimensional displacement ratio, defined as the displacement at the distal tip (δ_e) divided by the displacement at the base (δ_b), where the excitation is applied. In all cases, axial degrees of freedom of whole system (u) are unrestrained ($w = \psi = 0$), and the excitation is applied axially at the base.

The rationale behind choosing this non-dimensional parameter is the goal of maximizing output displacement to effectively remove calcified material, as discussed in the Introduction. For example, in an experimental study by Gavin [18], it was reported that applying an input displacement of 32 μm (δ_b) to a uniform wire resulted in an output displacement of 88 μ m (δ_e), yielding a displacement ratio of 2.75. However, it is important to note that this amplification occurred only at a specific wire length where the excitation frequency (23.5 kHz) coincided with the wire's natural frequency, a condition that could lead to fatigue-related issues. Outside of resonance conditions, the output displacement is typically less than the input due to energy dissipation along the wire. Additionally, it was demonstrated that an output displacement amplitude of 25 μ m at the distal tip of a straight, tapered wire is sufficient to penetrate calcified material, provided the geometry falls within certain design constraints. On the other hand, achieving larger input displacements requires more power from the piezoelectric actuator. Given the limitations in the design and manufacturing of ultrasonic generators, and the need to avoid resonance to prevent fatigue, it becomes essential to develop optimized wire geometries that achieve a higher output-to-input displacement ratio (δ_e/δ_b).

6.1. Parametric analysis

The parametric study is conducted for two main configurations: (i) a straight wire and (ii) a curved wire. In all case studies, both configurations include a tapered section. For the curved wire, the geometry consists of three segments (straight–curved–straight), as illustrated in Figure 3c and d, with constant curvature corresponding to a quarter-circle and a half-circle, respectively. Additionally, in the curved configuration, the taper is incorporated into the third (final) segment of the wire, as shown in Figure 2.

Figure 5 presents the frequency response results for the straight wire shown in Figure 2. Figure 5a shows the effect of l_f on the ratio of displacement at the distal tip to the base of the wire. In this case, the lengths of the taper section (l_t) and uniform section (l_e) are set to 0.2 m, with cross-section radii of 0.215 and 0.135 mm for h_f and h_e, respectively. It is evident that as the length of the wire increases, the response displacement decreases. Additionally, the number of maximum values (natural frequencies) increases with the length of the wire. This phenomenon can enhance the flexibility of the excitation frequency in practice, achieving the maximum improvement of movement at the distal tip of the wire relative to the excitation amplitude. However, it should be noted that this increase in length can also lead to greater fatigue compared to shorter wire lengths.

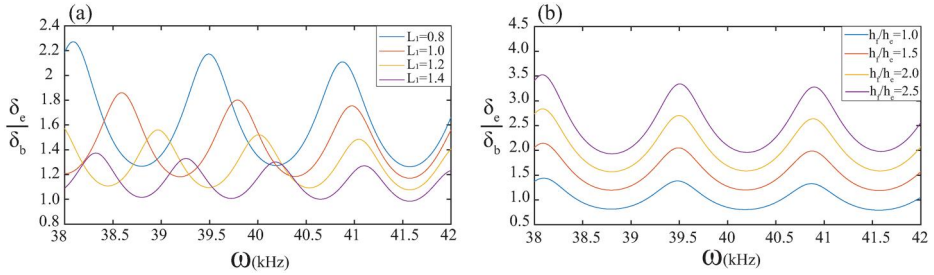

Figure 5. Steady-state frequency response of the distal tip-to-base displacement ratio for a straight wire with a tapered section, shown for varying (a) lengths (l_f) and (b) radius ratios (h_f/h_e), with fixed lengths for the second (l_t) and third (l_e) portions of the wire.

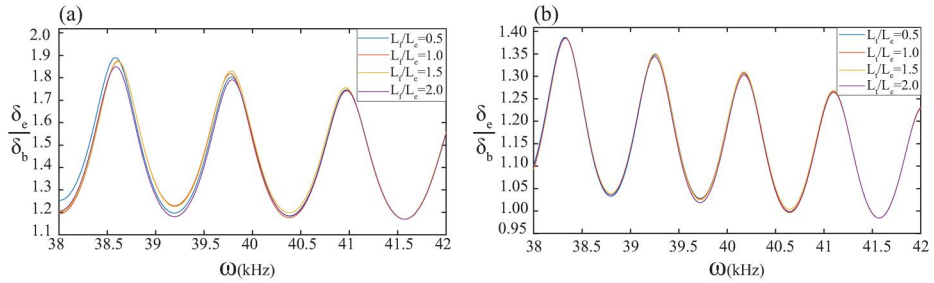

Figure 6. Steady-state frequency response of the distal tip-to-base displacement ratio for a straight wire with a tapered section, shown for different length ratios: (a) l_f/l_e and (b) l_t/l_e, with a constant total length of 1.2 m.

As part of Figure 5, Figure 5b shows the effect of varying the radius ratio (h_f/h_e) on the displacement ratio. In this case, l_f, l_t, and l_e are set to 1.2, 0.2, and 0.2 m, respectively. Additionally, h_f is set to 0.215 mm. The figure indicates that increasing the radius ratio amplifies the axial displacement at the distal tip of the wire. It is observed that for a completely uniform wire (blue line), the displacement ratio at the tip can be less than one, indicating a reduction in displacement amplitude compared to the excitation amplitude. However, a drawback of amplifying the displacement at the tip is the increased stress concentration at critical points, such as the start and end points of the tapered section.

Continuing the analysis, the effects of the length ratios l_f/l_e and l_t/l_e on the displacement ratio are investigated and presented in Figure 6. Figure 6a and b show the steady-state frequency response for these length ratios, respectively. The total length of the wire is set to 1.2 m, with radii of $h_f = 0.215$ mm and $h_e = 0.135$ mm. It can be concluded that variations in the length ratios of the wire do not significantly change the response at the distal tip. However, it is evident that the displacement ratio decreases at lower frequencies.

As part of the parametric study, three main investigations are conducted to examine the effects of varying the curvature angle, length ratio, and curvature radius on the displacement ratio, as shown in Figure 7a–c, respectively. It should be noted that in this section, based on Figure 3, the third part (L_3) includes the taper portion. To clarify the different portions of this part, L_{3f}, L_{3t}, and L_{3e} refer to the first uniform portion, the tapered section, and the last uniform portion of L_3, respectively.

Figure 7a shows the effect of varying the curvature angle on the displacement ratio. For this parametric study, the geometric parameters are set as $L_1 = 0.5$ m, $R = 0.2$ m, $L_{3f} = 0.3$ m, $L_{3t} = 0.1$ m, and $L_{3e} = 0.1$ m. It should be noted that the radii are set to $h_{3f} = 0.215$ mm and $h_{3e} = 0.135$ mm. Figure 7a indicates that the corresponding axial displacement at the distal tip of the wire decreases as the curvature angle increases. Additionally, with higher curvature angles, the number of natural frequencies occurring within the specified excitation frequency range increases.

In the parametric study of the curved wire, the length ratio of L_1/L_{3f} is varied to investigate its effect on the displacement ratio. The geometric parameters are set as $L_{3f} = 0.5$, $L_{3t} = 0.1$, $L_{3e} = 0.1$, $R = 0.2$, and $\theta = 90^\circ$. Figure 7b indicates that a higher length of L_1 compared to L_{3f} results in a significant decrease in the displacement at the distal tip of the wire relative to the excitation amplitude at the base of the wire. It is also evident that for specific length ratios (e.g., the blue line), the tip displacement can be smaller than the excitation amplitude, even in the presence of a taper section.

As the final case of the parametric study, Figure 7c shows the effect of varying the curvature radius on

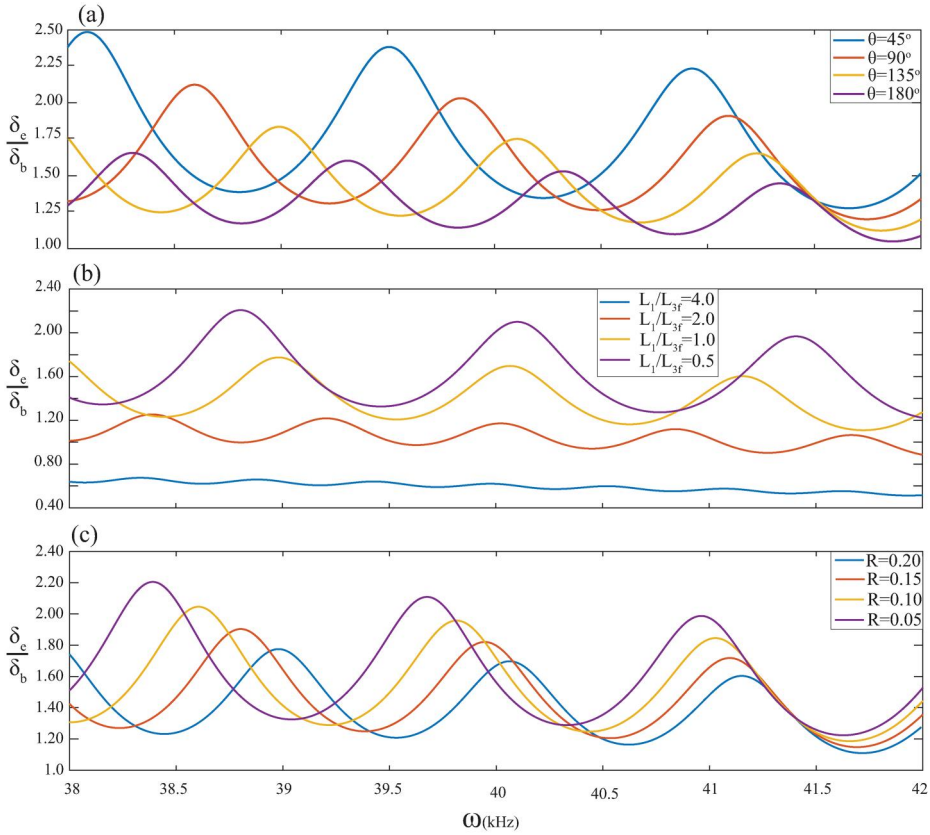

Figure 7. Steady-state frequency response of the distal tip-to-base displacement ratio for a curved wire with a tapered section, shown for different (a) curvature angles (θ) (where $L_1/L_{3f} = 5/3$ and $R = 0.2$), (b) length ratios (L_1/L_{3f}) (where $\theta = 90$ and $R = 0.2$), and (c) curvature radii (R) (where $L_1/L_{3f} = 1$ and $\theta = 90$).

the displacement ratio. For this case, the geometric parameters are set to $L_1 = 0.5$ m, $L_{3f} = 0.5$ m, $L_{3t} = 0.1$ m, $L_{3e} = 0.1$ m, and $\theta = 90^{\circ}$. The steady-state frequency response indicates that a larger curvature radius results in a lower ratio of distal tip displacement to excitation displacement. Based on the conducted parametric analysis, it seems essential to perform an optimization analysis to obtain the optimal values for the geometric parameters.

6.2. Design

A design step is performed in this section to determine the optimal values for the geometry parameters. It is evident from Figure 5b that a smaller radius ratio of l_e to l_f results in higher displacement at the tip of the wire compared to the input excitation. Therefore, for the design process, the radii of l_f and l_e are fixed at 0.215 and 0.0537 mm, respectively. However, to optimize the displacement ratio (δ_e/δ_b), two sets of design variables are defined: $[l_f/l_e,\ l_t/l_e]$ for straight wires and $[L_{3f}/L_{3e},\ L_{3t}/L_{3e}]$ for curved wires. The design study is conducted for straight and curved wires, as shown in Figure 8a and b, respectively, for various lengths of wire and curvature amounts.

In Figure 8, the right and left vertical axes represent the amplified displacements and the optimal length ratios, respectively. It should be noted that the excitation frequency in these cases is set to 40 kHz.

As shown in Figure 8a, for the straight wire, there is a significant difference between the optimal values of length ratios for various total lengths of wire. An important point highlighted here is that the assumption that increasing the wire length results in a decreased displacement ratio can be incorrect. By conducting a design optimization, the optimal length ratios can be determined, leading to an amplified base excitation amplitude.

Figure 8b presents the optimization results for the curved wire with various curvature angles, with the radius of curvature set to 0.2. In this design process, the geometry parameters are $L_1 = 1$ and $L_3 = 1$. The results indicate that for a wire with different curvature angles, the optimal values of $[L_{3f}/L_{3e},\ L_{3t}/L_{3e}]$ are approximately [1.75, 1.75]. Additionally, it can be concluded that for curvature angles less than 135°, the

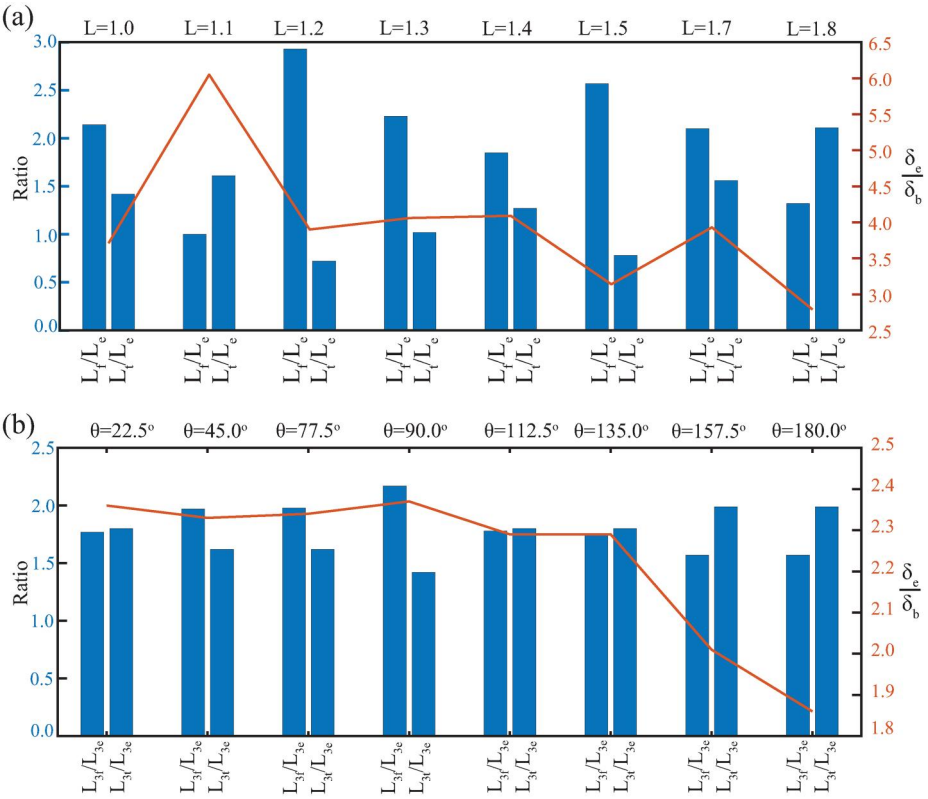

Figure 8. Design of (a) a straight wire for different total lengths (L), and (b) a curved wire for different curvature angles (θ), where in both cases the design variables are the length ratios of tapered section, optimized to maximize the distal tip-to-base displacement ratio.

displacement ratio can reach approximately 2.3 by optimizing the wire geometry.

In conclusion, based on the optimum values obtained to maximize the distal tip displacement, two critical factors contribute to the optimization from a structural dynamics perspective. First, the optimization process seeks geometric parameters that bring the natural frequency of the structure close to the excitation frequency of 40 kHz. As shown in the parametric analysis section, multiple natural frequencies are observed near this value, facilitating resonance. Second, it is important to consider the location of nodal points during wire vibration. The optimization aims to select geometric parameters that avoid placing the distal tip at or near a nodal point, ensuring that the tip experiences significant motion rather than remaining stationary.

7. Conclusion

In this paper, the dynamic behavior of curved wires is investigated with consideration of biomedical applications. The spectral Chebyshev technique is developed in conjunction with first-order shear deformation theory for beams to solve the integral boundary value problem derived from Hamilton's principle. This method is applied to straight, curved, and combined types of wires. The natural frequencies of each wire type are studied and compared to results from existing literature and finite element methods. Validation studies demonstrate that the presented spectral Chebyshev (SC) method can accurately predict the natural frequencies of wires with various geometries and boundary conditions.

In the second part of this study, various parametric studies are conducted to investigate the effects of geometric properties on the dynamic behavior of the wires. The steady-state frequency response of the wires is obtained, and the ratio of tip displacement to base excitation amplitude (δ_e/δ_b) is calculated and compared in the frequency range of 38 to 42 kHz. It is evident that including a tapered section in the wire geometry can amplify this ratio. The parametric study is conducted for two groups of wires: (i) straight wires with tapered sections and (ii) curved wires with a curved portion in the middle and a tapered section at the end.

For straight wires, the following conclusions are drawn:

- A higher length of wire results in a lower δ_e/δ_b ratio and a higher number of natural frequencies within the specified range.

- Increasing the radius ratio in the tapered section leads to a decrease in the δ_e/δ_b ratio.

For curved wires, the following conclusions are drawn:

- Higher curvature in the wire decreases the δ_e/δ_b ratio.
- A higher ratio of the first straight portion to the last straight portion of the wire significantly affects and decreases the δ_e/δ_b ratio.
- Lower radius values in the wire increase the δ_e/δ_b ratio.

Based on the parametric analysis, it was shown that displacement amplification is highly influenced by the geometry parameters. Therefore, as the final step of this paper, we conducted an optimization study to determine the optimal geometry parameters for maximizing the value of δ_e/δ_b. The optimization process was performed for both straight and curved wires. The design variables for each case are defined as the length ratio of the two uniform parts and the ratio of the tapered section length to the uniform portion length. For the straight wire, optimization was carried out for different lengths of wire. For the curved wire, the process was conducted for various curvature angles.

For the straight wire case study, it can be concluded that:

- The optimal length ratio of the first uniform portion to the end uniform portion should be greater than 1, indicating that the first portion should be longer.
- The mean value for the ratio of the taper section to the end uniform section length is approximately 1.

Furthermore, for the curved wire case study, it can be concluded that:

- By increasing the curvature amount, the δ_e/δ_b value decreases.
- The optimal values of the design variables, specifically the length ratios, are approximately in the range of 1.5 to 2 for all cases.

By comparing the design process between straight wire and curved wire, it can be concluded that the geometry parameters play a crucial role in increasing the displacement ratio. In straight wire, this ratio can increase by up to 600%, whereas in curved wire, it reaches up to 240%.

Acknowledgements

This work is funded under a DTIF award managed by the Department of Enterprise, Trade and Employment, Ireland and administered by Enterprise Ireland.

Disclosure statement

No potential conflict of interest was reported by the author(s).

References

[1] D. Dash, "Guidewire crossing techniques in coronary chronic total occlusion intervention: a to Z," *Indian Heart J.*, vol. 68, no. 3, pp. 410–420, 2016. DOI: 10.1016/j.ihj.2016.02.019.

[2] G. B. McGuinness, M. P. Wylie and G. P. Gavin, "Ablation of chronic total occlusions using kilohertz-frequency mechanical vibrations in minimally invasive angioplasty procedures," *Crit. Rev. Biomed. Eng.*, vol. 38, no. 6, pp. 511–531, 2010. DOI: 10.1615/CritRevBiomedEng.v38.i6.20.

[3] M. P. Wylie, G. B. McGuinness and G. P. Gavin, "Increased susceptibility of arterial tissue to wire perforation with the application of high-frequency mechanical vibrations," *IEEE Trans. Biomed. Eng.*, vol. 59, no. 4, pp. 1101–1108, 2012. DOI: 10.1109/TBME.2012.2184286.

[4] B. J. O'Daly, E. Morris, G. P. Gavin, C. O'Keane, J. M. O'Byrne and G. B. McGuinness, "High power, low frequency ultrasound: meniscal tissue interaction and ablation characteristics," *Ultrasound Med. Biol.*, vol. 37, no. 4, pp. 556–567, 2011. DOI: 10.1016/j.ultrasmedbio.2011.01.013.

[5] G. P. Gavin, G. B. McGuinness, F. Dolan and M. S. Hashmi, "Performance characteristics of a therapeutic ultrasound wire waveguide apparatus," *Int. J. Mech. Sci.*, vol. 49, no. 3, pp. 298–305, 2007. DOI: 10.1016/j.ijmecsci.2006.09.006.

[6] W. Tang, T. R. Wan, D. A. Gould, T. How, N. W. John, A stable and real-time nonlinear elastic approach to simulating guidewire and catheter insertions based on cosserat rod, *IEEE Trans. Biomed. Eng.*59 (8) (2012) 2211–2218. DOI: 10.1109/TBME.2012.2199319.

[7] T. Alderliesten, M. K. Konings and W. J. Niessen, "Modeling friction, intrinsic curvature, and rotation of guide wires for simulation of minimally invasive vascular interventions," *IEEE Trans. Biomed. Eng.*, vol. 54, no. 1, pp. 29–38, 2007. DOI: 10.1109/TBME.2006.886659.

[8] C. Zhang, Y. Cao, S. Liang and L. Feng, "Micro vibrations-based Friction Reduction Evaluation of Guide Wire for Endovascular Interventional Application," in *2021 WRC Symposium on Advanced Robotics and Automation, WRC SARA 2021*. Institute of Electrical and Electronics Engineers Inc., 2021, pp. 147–152. DOI: 10.1109/WRCSARA53879.2021.9612693.

[9] F. Berti, *et al.*, "Nickel-Titanium self-knotting suture wire for deep surgical field: a validated numerical

model," *Mater. Today Commun.*, vol. 24, pp. 101038, 2020. DOI: 10.1016/j.mtcomm.2020.101038.

[10] B. Konh, N. V. Datla and P. Hutapea, "Feasibility of shape memory alloy wire actuation for an active steerable cannula," *J. Med. Dev. Trans. ASME*, vol. 9, no. 2, pp.021002, 2015. DOI: 10.1115/1.4029557.

[11] C. Chapman, A. Eshghinejad and M. Elahinia, "Torsional behavior of NiTi wires and tubes: modeling and experimentation," *J. Intell. Mater. Syst. Struct.*, vol. 22, no. 11, pp. 1239–1248, 2011. DOI: 10.1177/1045389X11411224.

[12] M. Gannoun, M. L. Hellara, C. Bouby, T. Ben Zineb and T. Bouraoui, "Numerical simulation of the force generated by a superelastic NiTi orthodontic archwire during tooth alignment phase: comparison between different constitutive models," *Mater. Res. Express*, vol. 5, no. 4, pp. 045405, 2018. DOI: 10.1088/2053-1591/aaba4d.

[13] B. Bediz and O. B. Ozdoganlar, "Rotational dynamics of micro-scale cutting tools," *Precis. Eng.*, vol. 60, pp. 1–11, 2019. DOI: 10.1016/j.precisioneng.2019.07.004.

[14] B. Yagci, S. Filiz, L. L. Romero and O. B. Ozdoganlar, "A spectral-Tchebychev technique for solving linear and nonlinear beam equations," *J. Sound Vibr.*, vol. 321, no. 1–2, pp. 375–404, 2009. DOI: 10.1016/j.jsv.2008.09.040.

[15] F. Yang, R. Sedaghati and E. Esmailzadeh, "Free in-plane vibration of general curved beams using finite element method," *J. Sound Vibr.*, vol. 318, no. 4–5, pp. 850–867, 2008. DOI: 10.1016/j.jsv.2008.04.041.

[16] M. R. Anamagh and B. Bediz, "Three-dimensional dynamics of functionally graded and laminated doubly-curved composite structures having arbitrary geometries and boundary conditions," *Compos. Part B: Eng.*, vol. 172, pp. 533–546, 2019. DOI: 10.1016/j.compositesb.2019.05.087.

[17] H. Cao, M. H. Wu, F. Zhou, R. M. McMeeking and R. O. Ritchie, "The influence of mean strain on the high-cycle fatigue of Nitinol with application to medical devices," *J. Mech. Phys. Solids*, vol. 143, pp. 104057, 2020. DOI: 10.1016/j.jmps.2020.104057.

[18] G. P. Gavin, "Experimental and numerical investigation of therapeutic ultrasound angioplasty," Ph.D. thesis, Dublin City University, 2005.